ISSN (Print) 1226-1750
ISSN (Online) 2233-6656
Journal of Magnetics 23(1), 55-60 (2018) https://doi.org/10.4283/JMAG.2018.23.1.055

Rotor Open-Rib Design for Power Density Improvement in Synchronous Reluctance Motor

Jae-Kwang Lee[1], Dong-Hoon Jung[1], Jongsuk Lim[1], Ye Jun Oh[1], Ki-Doek Lee[2], and Ju Lee[1]*

[1]*Electrical Engineering, Hanyang University, Seoul 04763, Republic of Korea*
[2]*Intelligent Mechatronics Research Center, Korea Electronics Technology Institute, Bucheon 145052, Republic of Korea*

(Received 13 December 2017, Received in final form 22 March 2018, Accepted 22 March 2018)

MEPS are an efficiency regulation policy for induction motors, which are being implemented primarily in developed countries. Induction motors are the most commonly used type of motor in industry, owing to their simple structure and pricing advantages. Research on the efficiency improvement of induction motors has become saturated; therefore, studies to replace induction motors with SynRM have been actively conducted. SynRM is an electric motor driven by the inductance difference between the d-axis and the q-axis of the rotor, and has advantages of being composed of only an iron core and having a simple structure. Herein, we analyze the influence of the rotor shape on the inductance change. Further, the design for improving the output was implemented, and the solution to solve the stiffness problem that occurred as a result was studied. Finally, we confirmed the validity of the data through production and experiments.

Keywords : Minimum Energy Performance Standards (MEPS), rib, synchronous reluctance motor, 3D printing structure

1. Introduction

In developed countries, MEPS (minimum energy performance standards), which regulates the efficiency of induction motors, have been implemented. The MEPS improve the efficiency of power consumption by limiting the use of induction motors below the constant efficiency. To cope with this system, studies to improve the efficiency of induction motors have progressed actively, but they have now become saturated. Therefore, studies on synchronous reluctance motors (SynRM) to replace induction motors are being actively conducted. Generally, the SynRM rotor is composed of a barrier and a segment. As the number of barriers increases, the output density becomes larger. However, if a large number of barriers are deployed, the risk of scattering during high-speed rotation increases, and the rib and bridge are additionally arranged to prevent this. Herein, the effects of the bridges and ribs on the output are studied, and we proposed a design method to remove the rib and bridge to improve the output. However, a mechanical problem arises. To solve the problem, a structure made by three-dimensional (3D) printing was inserted. In addition, 3D electromagnetic field and 3D stiffness analyses were performed to confirm the design reliability. Finally, an experiment was conducted to validate the design model [1-3].

2. Principle of Synchronous Reluctance Motor

Figure 1 shows the design flow chart of the SynRM using 3D printing technology, which is divided into electrical and mechanical design. In the initial step, a detailed analysis of the existing models was conducted. The output, efficiency, and flux saturation were analyzed by 2D FEA. In addition, the flux saturation and leakage were analyzed in detail to reduce the output and increase the iron loss. To improve the output characteristics, a design that omits the rib and bridge structures was implemented. To solve the mechanical strength problem occurring at this time, 3D printing technology was included. A 3D FEA analysis was conducted to confirm the mechanical and electronic system output when the 3D printing technology was applied.

*Corresponding author: Tel: +82-2-2220-0342
Fax: +82-2-2295-7111, e-mail: julee@hanyang.ac.kr

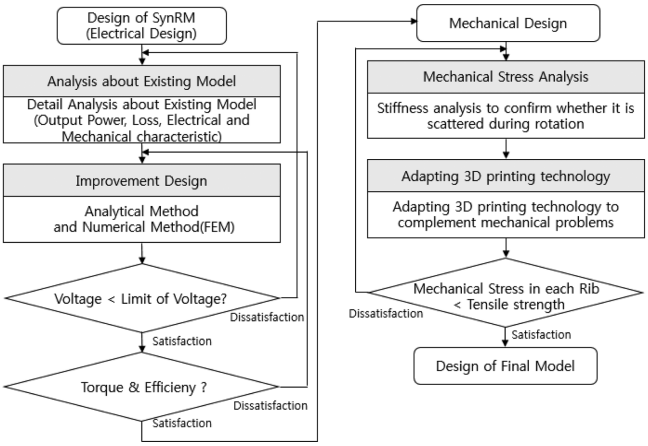

Fig. 1. Flow chart for the SynRM design using 3D-printed structure.

2.1. Principle of Synchronous Reluctance Motor

The output, efficiency, power factor, and THD are typical output characteristics for the SynRM. Eq. (1) is the torque equation of the SynRM. To maximize the output torque, a large difference between the d-axis inductance and the q-axis inductance must be designed. Eq. (2) is the power factor equation that shows the d-axis inductance and q-axis inductance as the primary factors.

$$T = \frac{3}{2} P_n (L_d - L_q) i_a^2 \frac{\sin 2\theta_i}{2} \tag{1}$$

$$PF = \left(\frac{L_d}{L_q} - 1\right) / \left(\frac{L_d}{L_q} + 1\right) \tag{2}$$

$$THD = \frac{\sqrt{E_2^2 + E_3^2 + E_4^2 + \cdots}}{E_1} \tag{3}$$

Eq. (3) is the total harmonic distortion (THD) of the induced voltage. If the THD is designed to be high because of the harmonic component, the torque ripple will be large during the actual operation. Therefore, when designing the SynRM, the THD should be lower.

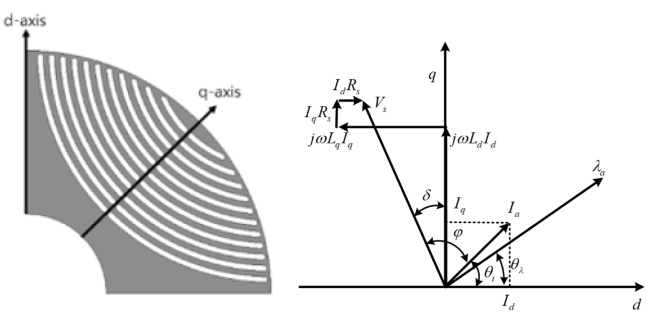

(a) (b)

Fig. 2. (a) d-axis, q-axis of SynRM. (b) Vector diagram of SynRM.

$$I_d = I_a \cos\theta_i \tag{4}$$

$$I_q = I_a \sin\theta_i \tag{5}$$

$$L_d = \frac{\lambda_a \cos\theta_\lambda}{I_d} \tag{6}$$

$$L_q = \frac{\lambda_a \sin\theta_\lambda}{I_q} \tag{7}$$

Eqs. (4) and (5) show the d-axis and q-axis currents, respectively. Eqs. (6) and (7) show the d-axis and q-axis inductances, respectively. The d-axis and q-axis inductances are derived from the phase angle of the input current and the magnitude and phase angle of the A-phase magnetic flux derived from FEM. Figure 2(a) shows the rotor shape of the d-axis and the q-axis, and Fig. 2(b) shows the vector diagram.

2.2. Analysis of Existing Model

Table 1 shows the input and output characteristics of the existing model. For the detailed analysis of the existing model, the d- and q-axis inductances were derived mathematically using Eqs. (4)-(7).

Figure 3 shows the rotor and stator of the existing model. To ensure mechanical rigidity, the existing model has a rib structure on the outside and a bridge structure on the inside. To improve the characteristics of the existing model, we analyzed its electromagnetic characteristics.

Figure 3(a) shows the result of the shape of the existing

Table 1. Output Characteristics of Existing Model.

Contents	Existing model	Unit
Rotating Speed	1500	RPM
Input Current	2.3	Arms
Torque	3.2	Nm
d-axis inductance	287.4	mH
q-axis inductance	73.6	mH
Efficiency	85.78	%

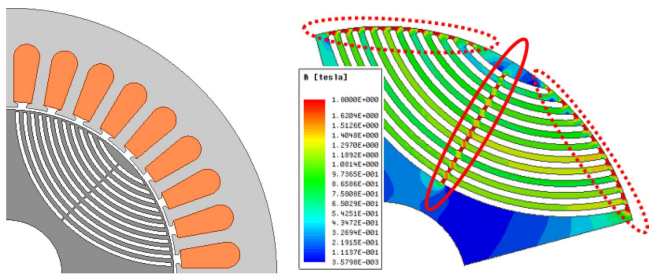

(a) (b)

Fig. 3. (a) Shape of existing model. (b) Rotor flux saturation of existing model.

model. Fig. 3(b) shows the rotor flux saturation; the part marked with a red dot is a rib structure; the part marked with a line is a bridge structure. It can be seen that the magnetic flux is saturated in the ribs and bridges. Consequently, magnetic flux saturation occurs, and a large amount of iron loss is expected to occur at this portion. Figure 3(b) shows a vector plot of the magnetic flux, which shows that many leaks occur. If a large amount of magnetic flux leakage occurs, the inductance difference between the d- and q-axis decreases; therefore, the output is reduced. In the next chapter, we will examine in detail the effects of the ribs and bridges on the output.

3. Analysis and Design of Rib and Bridge Structure

In the SynRM, the rib and bridge structures are essential structures for mechanical strength. However, owing to the rib and bridge structures, magnetic flux saturation and leakage occur, resulting in a decreased output. In this section, we analyze the effect of the rib and bridge structures on the d-axis and q-axis inductances using the magnetic equivalent circuit.

3.1. Specific Research on Bridge and Rib Structures

Figure 4 shows the magnetic equivalent circuit of the existing Rotor. Figure 4(a) is the d-axis circuit, Fig. 4(b) is the q-axis circuit. This magnetic equivalent circuit is based on three assumptions:

1) The flux leakage generated in the barrier is ignored.

2) The thickness of 1 to 5 barrier and segment shall be designed to be the same.

3) The local magnetic saturation phenomenon is ignored [3-5].

Eqs. (5), (6) express the magnetic resistance for each rotor part. As shown in Fig. 4, the d-axis circuit is composed of the magnetic resistance segment; the q-axis circuit is composed of the magnetic resistances of the barrier, rib, and bridge.

$$R_{seg1\sim n} = \frac{l_{seg1\sim n}}{\mu_{iron}\mu_o A_{seg1\sim n}},\ R_{barrier1\sim n} = \frac{l_{barrier1\sim n}}{\mu_{iron}\mu_o A_{barrier1\sim n}} \quad (8)$$

$$R_{rib1\sim n} = \frac{l_{rib1\sim n}}{\mu_{iron}\mu_o A_{rib1\sim n}},\ R_{bridge1\sim n} = \frac{l_{bridge1\sim n}}{\mu_{iron}\mu_o A_{bridge1\sim n}} \quad (9)$$

$$L_d = \frac{N^2}{R_{segment1\sim 5}} \quad (10)$$

$$L_q = \frac{N^2(R_{barrier1\sim n}+R_{rib1\sim n}+R_{bridge1\sim n})}{2R_{barrier1\sim n}R_{rib1\sim n}R_{bridge1\sim n}} \quad (11)$$

L_d is the d-axis inductance, and L_q is the q-axis inductance. If the barrier shape is fixed and L_d is fixed, the output should improve by reducing L_q. If the barrier shape is fixed, R_{rib}, and R_{bridge} are variables that can be adjusted to reduce L_q. To reduce L_q, the rib and bridge should be removed.

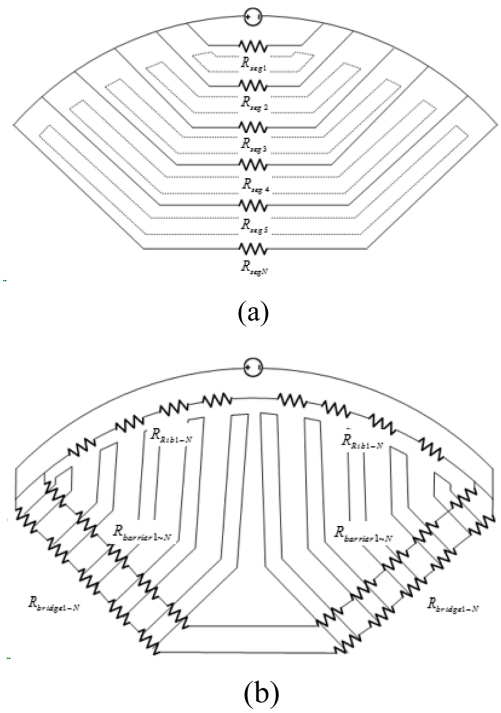

Fig. 4. Example of magnetic equivalent circuit. (a) d-axis. (b) q-axis.

3.2. Design for Improved Model

Figure 5(a) shows the rotor shape of the conventional model. As mentioned above, both the lip and bridge structures are included. Figure 5(c) show the process of deriving the final model. Figure 5(b) shows the removed bridge model that reduces flux leakage and prevents iron loss in the bridge of the existing model. Table 2 shows that the (b) model increased the output by 3.7 %. However, since the barrier shape is simple and has a circular structure, noise vibration may occur because of the tolerance when the 3D-printed structure is inserted. To compensate for the aforementioned disadvantages, model 1 adopts a W-type layer, a barrier is added to maximize the polarity, and the lip is omitted. Consequently, the output is improved by approximately 8.1 % compared with the existing model. The final model can predict mechanical vulnerability by omitting the rib. To solve the problem, we inserted the 3D-printed structure.

Table 2 shows the electromagnetic output characteristics of the existing model and the improved model. As shown in Table 2, the q-axis inductance is greatly reduced

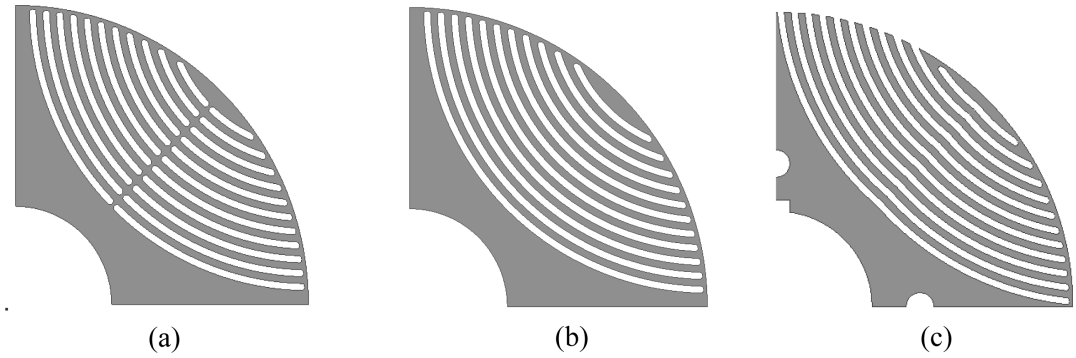

Fig. 5. Rotor shape of (a) existing model, (b) model 2 (removed bridge), (c) final model (adapted W-layer and removed rib).

Table 2. Output Characteristics.

Contents	(a)	(b)	(c)	Units
Rotating Speed		1500		RPM
Input Current		2.3		Arms
Torque	3.22	3.34	3.48	Nm
d-axis inductance	287.4	286.8	282.4	mH
q-axis inductance	73.6	65.2	53.1	mH
Output Power	506	525	547	W
Efficiency	85.7	86.2	86.7	%

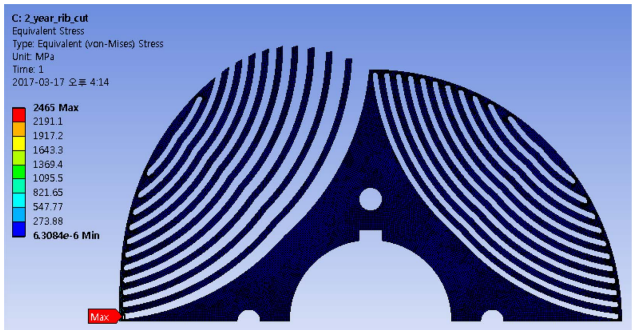

Fig. 6. (Color online) Mechanical stress of the improved model.

by the bridge and rib removal. Consequently, the output power is greatly improved by approximately 7 %. In addition, efficiency is improved by 1 %. Since the bridge and rib structures are removed, the risk of scattering during rotation is considerably higher.

Figure 6 shows the stiffness analysis results of the improved model: The stress is concentrated at the parts where the bridge and the rib are removed. The shear stress of the iron core material applied to this device is 265 MPa, but the concentrated stress is higher than 2000 Mpa, and we confirmed that the risk of scattering is very high. To solve this problem, the 3D printing technology was applied.

4. 3D Printing Structure for Improved Mechanical Strength

We confirmed that the primary characteristics of the motor have improved by the previous improvement design. However, a critical problem occurred, i.e., driving at a rated speed is difficult because of mechanical strength problems. To solve the problem, we combined the 3D printing technology with the SynRM [6]. Figure 8 shows the principle of combining the SynRM and the 3D-printed structures. To determine the material of the 3D printing injection, we studied polycarbon and ULTEM materials. ULTEM materials, as shown in Table 3, have excellent thermal deformation temperature and tensile strength; however, its manufacturing precision is poor. Polycarbon has excellent manufacturing precision, but its thermal deformation temperature and tensile strength are inferior to that of ULTEM. Therefore, polycarbon is the suitable material for this motor having a thin-layer structure of 1-mm thickness. The injection molding was

Table 3. Material Characteristics of 3D-Printed Structure.

Material	Poly Carbon	Ultem	Unit
Heat deflection temperature	133-138	167-216	°C
Tensile strength	57-58	71-81	Mpa
Degree of precision	0.9	0.7	mm

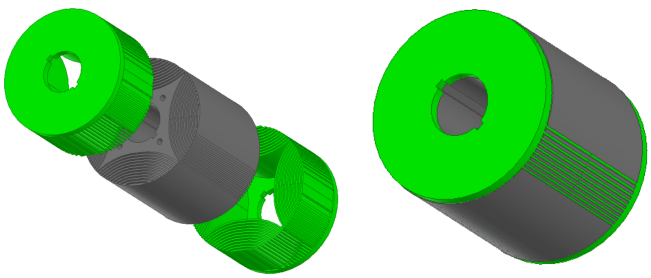

Fig. 7. (Color online) Rotor Shape with 3D-printed structure.

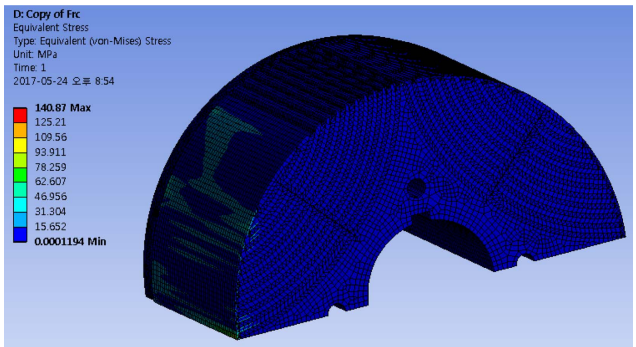

Fig. 8. (Color online) Mechanical stress of the improved model with 3D-printed structure.

inserted into the structure as shown in Figure 7. A 3D stiffness analysis was performed to confirm the strength after applying the 3D-printed structure.

Figure 8 shows the results of the 3D stiffness analysis: The maximum stress is 140 MPa and the safety factor is 1.7 or higher; therefore, the risk of scattering during rotation is low.

In addition, an electromagnetic 3D FEA analysis verifies whether the 3D-printed structure affects the electromagnetic characteristics. Table 4 shows the results before and after applying the 3D-printed structure. The results show that the influence of the 3D-printed structure on the electromagnetic field characteristics is very small.

5. Experiment

To validate the SynRM design method using the 3D-printed structure, the optimal model was fabricated and tested. Figure 9 shows the manufactured 3D-printed structure and the rotor shape. Figure 10 shows the test environment. Table 3 shows the results of the analysis and the test. The error is less than 3 %, and thus this study is validated.

6. Conclusion

Herein, a study was conducted to improve the output characteristics of existing models. The effect of the rib and bridge on the output was studied using the magnetic equivalent circuit. The design by removing the ribs and bridges has been implemented. Consequently, the output of the electromagnetic field has improved, but the mechanical strength has reduced.

To solve this problem, a 3D-printed structure was adopted and its characteristics were confirmed through the 3D FEA analysis of the electromagnetic field and mechanical strength. Finally, the study was validated through production and testing.

Table 4. Results of 3D FEA and Experiment.

Contents	3D FEA	Experiment	Unit
Rotating Speed	1500	1493	RPM
Input Current	2.3	2.4	Arms
Torque	3.48	3.49	Nm
Efficiency	86.5	86.0	%

Fig. 9. (Color online) Manufactured 3D-printed structure and rotor shape.

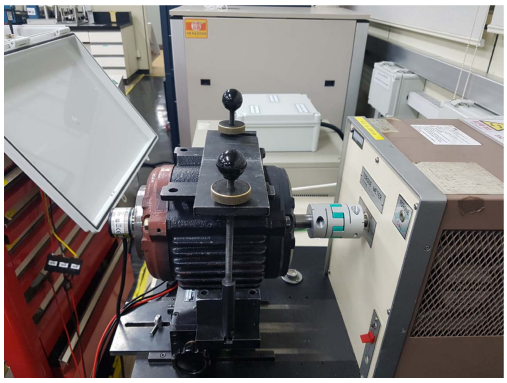

Fig. 10. (Color online) Test environment for the improved model.

Acknowledgment

This work was supported by the Human Resources Program in Energy Technology of the Korea Institute of Energy Technology Evaluation and Planning (KETEP), granted financial resource from the Ministry of Trade, Industry & Energy, Republic of Korea (No. 20174030201750).

This work was supported by the Korea Institute of Energy Technology Evaluation and Planning (KETEP) and the Ministry of Trade, Industry & Energy (MOTIE) of the Republic of Korea (No. 20162010104100).

References

[1] K.-C. Kim, J.-S. Ahn, S. H. Won, J.-P. Hong, and J. Lee, IEEE Trans. Magn. **43**, 2543 (2007).
[2] Gianmario Pellegrino, Francesco Cupertino, and Chris Gerada, IEEE Trans. Ind. Appl. **51**, 2 (2015).
[3] W.-H. Kim, K.-S. Kim, S.-J. Kim, D.-W. Kim, S.-C. Go, Y.-D. Chun, and J. Lee, IEEE Trans. Magn. **45**, 10 (2009).
[4] D.-H. Jung, Y. S. Kwak, J. Lee, and C.-S. Jin, IEEE Trans. Magn. **53**, 06 (2017).
[5] J.-K. Lee, D.-H. Jung, J. Lim, K.-D. Lee, and J. Lee, IEEE Trans. Magn. **54**, Article no. 8103005 (2018).
[6] H.-S. Hong, H.-C. Liu, S.-Y. Cho, J. Lee, and C.-S. Jin, IEEE Trans. Magn. **53**, 06 (2017).